# Dissipative Landau-Zener tunneling: crossover from weak to strong environment coupling

X. Dai,<sup>1,\*</sup> R. Trappen,<sup>1,\*</sup> H. Chen,<sup>2,3,†</sup> D. Melanson,<sup>1,‡</sup> M. A. Yurtalan,<sup>1,4</sup> D. M. Tennant,<sup>1,§</sup>

A. J. Martinez,<sup>1</sup> Y. Tang,<sup>1, ¶</sup> E. Mozgunov,<sup>5</sup> J. Gibson,<sup>6</sup> J. A. Grover,<sup>6</sup> S. M. Disseler,<sup>6</sup> J. I.

Basham,<sup>6</sup> S. Novikov,<sup>6</sup> R. Das,<sup>7</sup> A. J. Melville,<sup>7</sup> B. M. Niedzielski,<sup>7</sup> C. F. Hirjibehedin,<sup>7</sup> K. Serniak,<sup>7</sup>

S. J. Weber,<sup>7</sup> J. L. Yoder,<sup>7</sup> W. D. Oliver,<sup>7,8</sup> K. M. Zick,<sup>6</sup> D. A. Lidar,<sup>9</sup> and A. Lupascu<sup>1,10,\*\*</sup>

<sup>1</sup>Institute for Quantum Computing, and Department of Physics and Astronomy,

- University of Waterloo, Waterloo, ON, Canada N2L 3G1
  - <sup>2</sup>Center for Quantum Information Science & Technology.

University of Southern California, Los Angeles, California 90089, USA

<sup>3</sup>Department of Electrical & Computer Engineering,

University of Southern California, Los Angeles, California 90089, USA

<sup>4</sup>Department of Electrical and Computer Engineering,

University of Waterloo, Waterloo, ON, Canada N2L 3G1

<sup>5</sup>Information Sciences Institute, University of Southern California, Los Angeles, California 90089, USA

<sup>6</sup>Northrop Grumman Corporation, Linthicum, Maryland 21090, USA

<sup>7</sup>Lincoln Laboratory, Massachusetts Institute of Technology, Lexington, Massachusetts, 02421, USA

<sup>8</sup>Research Laboratory of Electronics, Massachusetts Institute of Technology, Cambridge, Massachusetts 02139, USA

<sup>9</sup>Departments of Electrical & Computer Engineering, Chemistry,

and Physics, and Center for Quantum Information Science & Technology,

University of Southern California, Los Angeles, California 90089, USA

<sup>10</sup> Waterloo Institute for Nanotechnology, University of Waterloo, Waterloo, ON, Canada N2L 3G1

(Dated: July 6, 2022)

Landau-Zener (LZ) tunneling [1], describing transitions in a two-level system during a sweep through an anti-crossing, is a model applicable to a wide range of physical phenomena, such as atomic collisions [2], chemical reactions [3], and molecular magnets [4], and has been extensively studied theoretically and experimentally [5– 11]. Dissipation due to coupling between the system and environment is an important factor in determining the transition rates. Here we report experimental results on the dissipative LZ transition. Using a tunable superconducting flux qubit, we observe for the first time the crossover from weak to strong coupling to the environment. The weak coupling limit corresponds to small system-environment coupling and leads to environmentinduced thermalization. In the strong coupling limit, environmental excitations dress the system and transitions occur between the dressed states. Our results confirm previous theoretical studies of dissipative LZ tunneling in the weak and strong coupling limits [5, 12]. Our results for the intermediate regime are novel and could stimulate further theoretical development of open sys-

\*\* adrian.lupascu@uwaterloo.ca

tem dynamics [13]. This work provides insight into the role of open system effects on quantum annealing, which employs quantum tunneling to search for low-energy solutions to hard computational problems [14, 15].

LZ tunneling describes non-adiabatic transitions through an anti-crossing using a two-state quantum system with a linearly changing energy separation. In the closed-system case, analytical solutions for transition probabilities were obtained in Ref. [1]. In the opensystem case, analytical results have been obtained using the spin-boson formalism [13] in various limiting cases for the temperature and coupling strength of the environment [5, 6, 16]. More recently, LZ transitions have been studied in relation to quantum annealing [17, 18], where non-adiabatic transitions between the ground and excited states of a multispin system are potential bottlenecks for the computational power.

The LZ transition was observed experimentally in various physical systems including superconducting circuits [7], Bose-Einstein condensates [8], single-molecule magnets [9], Rydberg atoms [10] and mixed-valence complexes [11]. In superconducting circuit experiments, LZ transitions have been used to demonstrate phase coherence [7, 19], to realize quantum gates [20] and to validate theories of macroscopic resonant tunneling (MRT) in the presence of strong 1/f noise [21, 22]. These experiments were either analyzed based on weak coupling open system effects with effective coherence parameters, or are limited to the strong-coupling limit.

Our experiments are performed using a two-level quantum system implemented using a tunable superconducting flux qubit. A schematic of the experiment setup is shown in Figure 1(a). The qubit circuit consists of

<sup>\*</sup> These two authors contributed equally. x35dai@uwaterloo.ca, rtrappen@uwaterloo.ca

<sup>&</sup>lt;sup>†</sup> Current address: Lawrence Berkeley National Laboratory, Berkeley, CA 94720, USA

<sup>&</sup>lt;sup>‡</sup> Current address: Department of Engineering Physics, McMaster University, 1280 Main St., Hamilton, Ontario, Canada L8S 4L8

 $<sup>\</sup>S$ Current address: Lawrence Livermore National Laboratory, Livermore, California, 94550, USA

<sup>&</sup>lt;sup>¶</sup> Current address: 1QB Information Technologies (1QBit), Vancouver, BC, Canada V6E 4B1

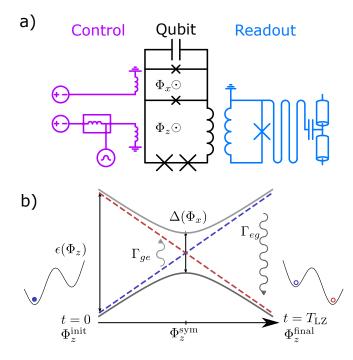


FIG. 1. The flux qubit and the dissipative LZ transition. (a) Schematic of the tunable capacitively-shunted flux qubit and the control and readout circuitry. The flux biases  $\Phi_x, \Phi_z$ are each supplied by a DC voltage source and the  $\Phi_z$  is further controlled by a fast arbitrary waveform generator, joined to the DC control through a bias-tee. Readout is done by measuring the transmission through an rf-SQUID terminated waveguide resonator coupled inductively to the qubit. (b) Schematic representation of the LZ sequence. The blue and red dashed lines indicate the energies of the diabatic states, which are separated by  $2I_p(\Phi_z - \Phi_z^{\text{sym}})$ . The grey lines indicate the eigenenergies of the qubit, which has a minimum gap of  $\Delta$  at the symmetry point  $\Phi_z^{\text{sym}}$ . The curly arrows indicate the dominant open system effects in the LZ measurements in the weak-coupling limit, which are excitations around the symmetry point and relaxation after the symmetry point. The double-well plots on either side of the energy level diagram are a representation of the qubit potential at the beginning and end of the LZ sweep.

two flux loops, designated as z, x respectively, including Josephson tunnel junctions. Under suitable flux bias conditions, the circuit has a double-well potential energy landscape, with the two wells corresponding to persistent current flowing in opposite directions in the z loop. At low energy, the system is confined to the ground states of the two wells, described by the two-state (qubit) Hamiltonian

$$H_q = -\frac{\epsilon(\Phi_z)}{2}\sigma_z - \frac{\Delta(\Phi_x)}{2}\sigma_x,\qquad(1)$$

with  $\sigma_{z,x}$  being the Pauli operators. Here  $\epsilon = I_p(\Phi_z - \Phi_z^{\text{sym}})$  and  $\Delta$  are respectively the bias and tunnelling amplitude between persistent current states,  $I_p$  is the persistent current,  $\Phi_{z(x)}$  is the flux bias in the z(x) loop,

and  $\Phi_z^{\text{sym}}$  is the  $\Phi_z$  bias which gives a symmetric doublewell potential. The  $\Phi_x, \Phi_z$  biases are controlled by DC voltage sources and the  $\Phi_z$  bias is additionally coupled to a fast arbitrary waveform generator (AWG), combined with the DC control through a bias-tee. Readout of persistent current states is done by inductively coupling the qubit z loop to a flux-sensitive resonator. The circuit is also capacitively coupled to a waveguide used to send microwave signals, allowing resonant excitation of the circuit. Spectroscopically measured transition frequencies are fit using a circuit network model, which allows for finding the circuit parameters (Supplementary Information). The two-state model parameters  $I_p$  and  $\Delta$  can then be obtained from the circuit model at arbitrary flux bias near the symmetry point  $\Phi_z = \Phi_z^{\text{sym}}$ .

A diagram representation for the LZ measurement is shown in Figure 1(b). At t = 0, the qubit is prepared in the left well at  $\Phi_z^{\text{init}} \approx -0.005 \Phi_0 + \Phi_z^{\text{sym}}$ . Then the qubit z flux  $\Phi_z$  is linearly swept to  $\Phi_z^{\text{final}} \approx 0.005 \Phi_0 + \Phi_z^{\text{sym}}$  over the duration  $T_{\text{LZ}}$ . The initial and final values of  $\Phi_z$  ensure the LZ sweep starts and ends far enough from the anti-crossing so that the qubit energy eigenstates approximately overlap with the persistent current states. The qubit state population after the sweep is read out by measuring the state dependent transmission through the resonator (Supplementary Information). The sequence is repeated for a range of  $\Phi_x$  and  $T_{\text{LZ}}$  values. With decreasing  $\Phi_x$ ,  $\Delta$  decreases nearly exponentially whereas  $I_p$  increases by about 10% over the entire range.

The measured final excited state probabilities  $P_e$  versus  $T_{\rm LZ}$  at short times are shown in Figure 2(a). In the weak-coupling limit, the system is expected to behave nearly coherently for short sweep times, implying that the final excited state probabilities are well described by the LZ formula

$$P_{\rm LZ} = \exp\left(-\frac{\pi\Delta^2}{2\hbar v}\right),\tag{2}$$

where v is the sweep velocity, given by  $v = 2I_p(\Phi_z^{\text{final}} - \Phi_z^{\text{init}})/T_{\text{LZ}}$ . To confirm the coherent-limit behaviour, we fit an exponential decay to the short time decay of the measured final excited probabilities, and then convert the decay constant to an effective gap  $\Delta_{\text{LZ}}$  assuming  $I_p$  given by the circuit model. The extracted values of the effective gap  $\Delta_{\text{LZ}}$  are compared to values of  $\Delta$  given by the circuit model in Figure 2(b). There is excellent agreement for the full range of  $\Phi_x$  measured in LZ experiments, with  $\Delta$  in the range of 12 - 120 MHz.

After confirming the short-time behaviour, we observe the dynamics at longer sweep times, where coupling to the environment is expected to affect the LZ transition. We first discuss the characterization of the environment. Measurement of the noise spectrum is done based on its effect on qubit relaxation and dephasing at  $\Delta/h \gtrsim 1$  GHz, where the weak coupling limit holds. We find that the coherence is flux noise limited and can be explained by a noise power spectral density (PSD) consistent with previous work [23–25], where the noise power varies to a

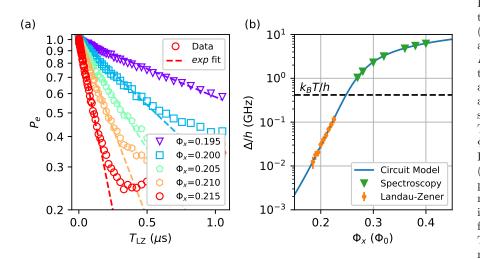


FIG. 2. LZ data in the short sweep time range and fitted effective gap. (a) Experimental data (open markers) and exponential fits (dashed lines) to  $P_e$  versus  $T_{LZ}$ . The maximum sweep time included in the fit is determined adaptively, by first starting from 30 ns and then increasing until the mean square loss of the fit exceeds 0.01. (b) The minimum gap  $\Delta$  versus x-bias flux  $\Phi_x$  from spectroscopy (green triangle), LZ (orange dots) and circuit model (blue line). Errors in the LZ data are propagated from errors of the exponential decay fit. The circuit model is a result of fitting spectroscopy data for a range of  $\Phi_x$ ,  $\Phi_z$  (not shown here). The black dashed line indicates the noise temperature, which is assumed to be the base temperature of the dilution fridge,  $T = 20 \,\mathrm{mK}$ .

good approximation as 1/f, with f the frequency, up to 1 GHz, combined with quasi-ohmic noise at higher frequencies. Our noise measurements, which are sensitive to the symmetrized noise power, combined with the assumption that the environment is in thermal equilibrium at the fridge base temperature, allow us to write the quantum noise PSD as

$$S_{\lambda}(\omega) = S_{\lambda,1/f}(\omega) + S_{\lambda,\text{ohmic}}(\omega), \qquad (3)$$

$$S_{\lambda,1/f}(\omega) = \frac{A_{\lambda}\omega}{|\omega|^{\alpha}} \left[ 1 + \coth\left(\frac{\beta\hbar\omega}{2}\right) \right] \text{ and } \qquad (4)$$

$$S_{\lambda,\text{ohmic}}(\omega) = B_{\lambda}\omega|\omega|^{\gamma-1} \left[1 + \coth\left(\frac{\beta\hbar\omega}{2}\right)\right], \quad (5)$$

with  $\lambda \in \{\Phi_x, \Phi_z\}$ . Here  $\beta = 1/k_BT$  is the inverse temperature and  $A_{\lambda}(B_{\lambda})$  and  $\alpha(\gamma)$  characterize the strength and frequency dependence of the 1/f (quasi-ohmic) component respectively (Supplementary Information). Given the smaller noise power and coupling matrix elements of the  $\Phi_x$  noise for flux biases probed in the LZ measurement, we only consider  $\Phi_z$  noise from here onward.

The measured final ground state probabilities  $P_g = 1 - P_e$  for different  $\Phi_x$  are shown in Figure 3(a,b), versus the full range of sweep time  $T_{\rm LZ}$  and the dimensionless time  $\tau = \Delta^2/\hbar v$ , with  $\Delta$  being the predicted value from the circuit model. Analyzing the dependence on both the actual time  $T_{\rm LZ}$ , and dimensionless time  $\tau$  allows us to make complementary observations about the changes in the effect of the environment as  $\Phi_x$ , or equivalently  $\Delta$ , is tuned.

The weak-coupling limit between the system and the environment is expected to apply when the systemenvironment coupling strength is much smaller than the system's own energy scale, in this case  $\Delta$ . In the weak coupling limit, the adiabatic master equation (AME) [26] can be applied, where the dominant environmental effects are thermal transitions and decoherence between the energy eigenstates of the system. The AME-simulated final ground state probabilities are shown in Figure 3(c,d). For large  $\Phi_x$ ,  $P_q$  increases non-monotonically with  $T_{LZ}$ . This can be explained by competition between thermal excitation around the minimum gap and relaxation after the minimum gap at intermediate and long time scales [12]. As the total sweep time increases,  $P_g$  first increases following the coherent limit, until the qubit has enough time to thermalize around the minimum gap and  $P_g$  starts to decrease. Further increase of the total sweep time allows the qubit to relax after crossing the minimum gap, increasing the final ground state probabilities again. The timescale required to thermalize at the minimum gap is small compared to that after the minimum gap, since  $\Phi_z$  noise couples the energy eigenstates most strongly at the minimum gap. For smaller  $\Phi_x$ , the thermalization timescale at the minimum gap becomes smaller than the system's coherence time, hence  $P_q$  reaches 0.5 faster than the coherent limit, and then increases gradually afterwards due to slow thermal relaxation after the gap.

Comparing the experimental data and AME simulation, we find qualitative agreement at large  $\Phi_x$ . The experimental data show smaller  $P_g$  local maxima, which could indicate that the noise experienced by the qubit in LZ sweep is larger than the extrapolated noise values based on qubit decoherence measurements. There is significant disagreement between the data and the AME simulation at smaller  $\Phi_x$ . Looking at the  $T_{\rm LZ}$  dependence, while the AME predicts  $P_g$  to nearly settle at 0.5, the experimental data shows  $P_g$  to continue increasing with increasing sweep time. In fact, the experiment final ground state probability  $P_g$  for different  $\Phi_x$  crosses at long times and the highest  $P_g$  is obtained at the lowest  $\Phi_x$ . Furthermore, when looking at the  $\tau$  dependence, it

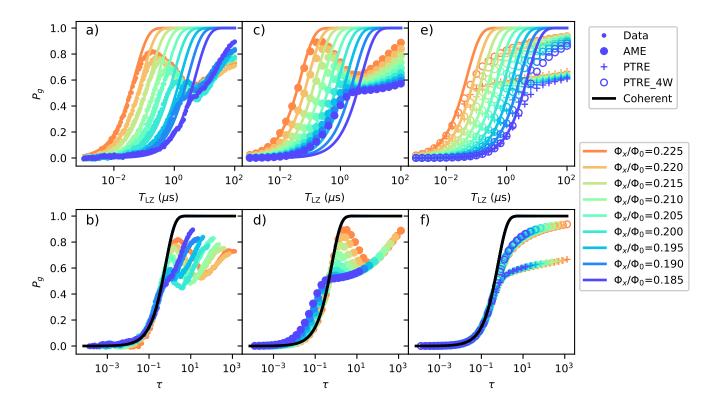


FIG. 3. LZ data for the full range of  $\Phi_x$  and sweep time, and comparison with simulation. Final ground-state probability  $P_g$  versus the sweep time  $T_{\rm LZ}$  (top) and the dimensionless sweep time  $\tau = \Delta^2/\hbar v$  (bottom), for (a, b) experimental data, (c,d) Adiabatic master equation simulation (labeled as AME) results with nominal noise parameters and (e,f) Polaron-transformed Redfield equation simulation with nominal noise parameters (labeled as PTRE) and 4 times larger MRT width W (labeled as PTRE\_4W). All panels also contain the coherent limit given by  $P_g = 1 - P_{\rm LZ}$ .

can be seen that for  $\tau \gg 1$ , where relaxation after the gap is expected to dominate, the simulated  $P_g$  curves for different  $\Phi_x$  collapse onto the same  $\tau$  dependence. This is contrasted with experimental data, where the  $P_g$  curves shift left towards the coherent limit as  $\Phi_x$  is reduced. These signatures indicate that the weak-coupling limit breaks down as the minimum gap  $\Delta$  is reduced.

To understand the data in the strong-coupling limit, the polaron-transformed master equation (PTRE) is used [27, 28]. PTRE incorporates strong systemenvironment coupling by transforming into the dressed polaron frame and treats the tunneling parameter  $\Delta$  perturbatively. The noise PSD in the polaron frame is separated into low- and high- frequency components. Particularly, the low frequency part is characterized by two parameters,

$$W^2 = 2I_p^2 \int \frac{d\omega}{2\pi} S^+_{\Phi_z,1/f}(\omega), \text{ and} \qquad (6)$$

$$\epsilon_p = 2I_p^2 \int \frac{d\omega}{2\pi} \frac{S^-_{\Phi_z,1/f}(\omega)}{\hbar\omega},\tag{7}$$

which are known as the MRT width and reorganization energy respectively [21]. The functions  $S_{\Phi_*}^{-(+)}$  are the

(anti-) symmetrized low frequency  $\Phi_z$  noise. The PTRE is expected to hold when the environment-induced dephasing is much larger than the qubit's minimum energy gap, or  $W \gg \Delta$ . By integrating the 1/f noise obtained from dephasing time measurements, we obtain  $W/h \approx 48 - 59$  MHz. Assuming the environment is in thermal equilibrium,  $\epsilon_p$  is related to W via the fluctuation-dissipation theorem  $\epsilon_p = W^2/2k_BT$ . The result of PTRE simulations is shown in Figure 3(e,f). The final ground-state probability  $P_g$  first increases with increasing sweep time, closely following the coherent LZ probabilities until around  $P_g = 0.5$  where it flattens. It is found through numerical experiment that increasing W while keeping T unchanged, or equivalently increasing  $\epsilon_p/W$ , brings the PTRE results closer to the coherent LZ probabilities. In fact, it has been demonstrated previously that for a flux qubit strongly coupled to low frequency noise, the LZ transition probability recovers the coherent LZ probability when  $\epsilon_p \gg W$  [22].

In the experimental data, the transition probabilities approach the coherent limit as  $\Phi_x$  or  $\Delta$  is reduced, indicating strong coupling between the qubit and the environment. At the smallest  $\Phi_x$ , the measured  $P_g$  does not flatten near 0.5, contrasting the PTRE prediction with nominal noise values, but is closer to the PTRE prediction with larger MRT width W. This suggests that the noise seen by the qubit is larger than the integrated 1/fnoise. This is not entirely surprising, given that previous MRT measurements on superconducting flux qubits also revealed larger W than the integrated power of 1/f flux noise (Supplementary Information).

The dissipative LZ transition studied here can be considered a toy-model for dynamics in quantum annealing, where small gap anti-crossings between the lowest two energy eigenstates are expected to play an important role [17, 29]. Our results thus contribute to the understanding of the role of open system effects in a quantum annealer [29-33]. In the weak-coupling limit, despite the fact that the AME predicts an improvement in the final ground state probabilities in the small-gap, fast-sweep regime, realizing this experimentally requires further noise reduction, as needed to preserve the validity of the weak-coupling limit for smaller gaps. However, as the system scales up, noise in the system is expected to increase and the minimum gap to close, making the weak-coupling limit hard to achieve for large annealers. On the other hand, remaining in the strong coupling limit is not necessarily detrimental, as the experimental data and PTRE simulation show a counter-intuitive result that higher ground state probabilities can be achieved in the intermediate to strong coupling limit, as compared to the weak-coupling limit, when  $\epsilon_p/W$  is large enough. It should be noted that coupling to classical noise gives  $\epsilon_p = 0$ , which would limit the maximum  $P_g$  to 0.5.

In summary, we experimentally characterized the LZ transition probability in a superconducting flux qubit with a wide range of sweep velocities v and minimum gap sizes  $\Delta$ , and we showed a crossover from weak to strong coupling to flux noise. We found that for large gap  $\Delta$ , the competition between adiabaticity and environmentinduced thermalization leads to non-monotonic dependence of the final ground state probability  $P_a$  on sweep time, which can be reproduced by a weak-coupling model, the AME. However, as  $\Delta$  becomes smaller, the nonmonotonicity gradually disappears and  $P_q$  becomes closer to the coherent LZ transition rate, which is consistent with a strong-coupling model, the PTRE. These findings confirm previous analytical and numerical results on the dissipative LZ dynamics in the weak- and strong-coupling limit. The data in the crossover regime are expected to stimulate further theoretical developments of open system dynamics. The LZ problem is a relevant model for dynamics in a large scale quantum annealer. Possible future extensions of this work include the investigation of the crossover region in multi-qubit settings and the use of environments with specifically designed noise coupling axis and noise power for improved quantum information processing.

## ACKNOWLEDGMENTS

We thank the members of the Quantum Enhanced Optimization (QEO)/Quantum Annealing Feasibility Study (QAFS) collaboration for various contributions that impacted this research. In particular, we thank D. Ferguson for fruitful discussions of experiments, A. J. Kerman for guidance on circuit simulations and design, and R. Yang for related work on circuit modelling and useful discussions. We gratefully acknowledge the MIT Lincoln Laboratory design, fabrication, packaging, and testing personnel for valuable technical assistance. The research is based upon work supported by the Office of the Director of National Intelligence (ODNI), Intelligence Advanced Research Projects Activity (IARPA) and the Defense Advanced Research Projects Agency (DARPA), via the U.S. Army Research Office contract W911NF-17-C-0050. The views and conclusions contained herein are those of the authors and should not be interpreted as necessarily representing the official policies or endorsements, either expressed or implied, of the ODNI, IARPA, DARPA, or the U.S. Government. The U.S. Government is authorized to reproduce and distribute reprints for Governmental purposes notwithstanding any copyright annotation thereon.

## AUTHOR CONTRIBUTIONS

R.T. performed the experiments. R.T. and X.D. performed the data analysis. X.D. performed the numerical simulations. H.C. provided guidance on the numerical simulations and theoretical models. D.M., M.A.Y., A.J.Martinez, and Y.T. designed the device. S.N. provided feedback on device design. E. M. explored alternative explanation of the experimental data within the AME model. J.G. J.A.G. and X.D. performed earlier versions of the experiments on a different device and setup. D.M.T., J.A.G., S.D. and J.B. contributed to the development of the experiment infrastructure. R.D., A.J.Melville, B.M.N. and J.L.Y. developed the fabrication process and fabricated the device. C.H., K.S., S.J.W. contributed to fridge and electronics operation. W.O. supervised the QEO/QAFS effort from Lincoln lab, K.M.Z. led the coordination of the QEO/QAFS experimental effort, D.L. led the QEO/QAFS program and A.L. conceived and supervised this work. All authors were involved in the discussion of experiments and data analysis. X.D., R.T and A.L. wrote the paper with feedback from all authors.

### COMPETING INTERESTS

The authors declare no competing interests.

#### METHODS

#### A. Device fabrication

The device is fabricated at MIT Lincoln Laboratory using a multi-tier fabrication process, which consists of a high-coherence qubit tier, an interposer and a multi-layer control tier [34, 35]. Our device only uses the qubit and interposer tier. The qubit tier contains high quality Al forming the qubit loop and capacitance, as well as  $Al/AlO_x/Al$  junctions. The interposer tier contains the tunable resonator and the control lines. They are bump bonded together in a flip-chip configuration using indium bumps.

#### B. Qubit control and readout

The qubit x, z flux biases are each controlled using onchip flux bias lines, with current supplied by a DC voltage source and a fast AWG. The DC source has stronger coupling to the qubit loops to achieve flux biasing of more than a flux quantum. The AWG has weaker coupling to the flux biases, corresponding to a bias range of about 100 m $\Phi_0$ .

Before the LZ sweep, the qubit needs to be prepared in its ground state. Passive cooling is not possible when the tunneling barrier between persistent current states is large. We use a cooling protocol similar to that demonstrated in Ref. [36]. Using the large tunneling amplitude between the ground state of the higher well and the excited state of the opposite well, residual excited populations can be adiabatically transferred to the lower well and the system quickly relaxes to the ground state. Additional details of the energy spectrum and this cooling method is discussed in the Supplementary information.

The qubit state is read by measuring the statedependent transmission through the tunable resonator. When doing spectroscopy and coherence measurements, the resonator is biased at a flux-insensitive position (0 flux in the SQUID), and readout is in the qubit energy eigenbasis, due to dispersive interaction between the qubit and resonator. During the LZ measurement, the resonator is biased at a flux-sensitive position ( $-0.15 \Phi_0$ flux in the SQUID), which allows measuring the qubit's persistent current states. Since the readout point of the LZ experiment is far from the qubit's symmetry point, the persistent current basis and energy eigenbasis of the qubit nearly coincide, with more than 99% overlap, and we do not distinguish the two bases at the readout point.

#### C. Noise characterization

The qubit is capacitively coupled to a microwave line. This allows spectroscopy, qubit relaxation (T1) and qubit dephasing (T2) measurement when  $\Delta/h \gtrsim 1$  GHz. The flux-dependent qubit transition frequencies are used to fit a complete circuit model of the device, which is used to compute  $I_p$  and  $\Delta$  at different  $\Phi_x$  [37]. The circuit model is also used to compute the noise sensitivity of the qubit at different flux biases. Combining the noise sensitivity with the T1, T2 measurement results allows us to determine the noise PSD, which is used in the master equation simulation for LZ transition. More details of the noise parameters are given in the Supplementary Information.

#### D. Master equation simulation

The master equation simulations were performed using HOQST, a Julia package for open system dynamics with time-dependent Hamiltonians [27]. The simulation takes the qubit Hamiltonian in Eq. (1), with  $I_p$ ,  $\Delta$  given by the circuit model. The qubit-bath interaction considered is

$$H_{\rm int} = -I_p \sigma_z \otimes Q, \tag{8}$$

where  $\sigma_z$  acts on the qubit and Q acts on the environment degrees of freedom which causes the qubit z loop flux noise.

The AME is a completely-positive time-dependent version of the frequency form Redfield equation. Although a rigorous upper bound on the error of the AME is only small in the adiabatic limit [38], it is likely that the error is still small in the non-adiabatic limit. Specifically, the form used in this work is the double-sided AME without the Lamb-shift terms [26], given by

$$\begin{split} \dot{\rho}_q(t) &= -\frac{i}{\hbar} [H_q(t), \rho_q(t)] \\ &+ \frac{1}{\hbar^2} \sum_{\omega} S_{\Phi_z}(\omega) \left[ L_{\omega}(t) \rho_q L_{\omega}^{\dagger}(t) - \frac{1}{2} \left\{ L_{\omega}^{\dagger}(t) L_{\omega}(t), \rho_q(t) \right\} \right], \end{split}$$

where  $\rho_q$  is the density matrix of the qubit and  $S_{\Phi_z}$  is the power spectral density of the z loop flux noise. The Lindblad operators  $L_{\omega}$  are given by

$$L_{\omega}(t) = \sum_{E_{\beta} - E_{\alpha} = \omega} \langle \alpha(t) | I_p \sigma_z | \beta(t) \rangle | \alpha(t) \rangle \langle \beta(t) |, \qquad (9)$$

where  $E_{\alpha(\beta)}$  and  $|\alpha(\beta)\rangle$  are the system's instantaneous energy eigenvalues and eigenstates, and  $\alpha, \beta \in \{g, e\}$ . Numerical experiments show that including the Lamb shift terms has a negligible impact on the final groundstate probabilities.

The PTRE is a model that accounts for strong systemenvironment coupling and has found to explain experimental data in quantum annealers coupled strongly to low frequency noise [22, 28]. PTRE has the same functional form as the AME but with the Hamiltonian, Lindblad operators and noise PSD given in the polaron frame. Using tilde to denote the polaron frame, we have

$$\tilde{H}_q = -I_p (\Phi_z - \Phi_z^{\text{sym}}) \sigma_z, \qquad (10)$$

$$\tilde{L}_{\omega,\lambda\in\{+,-\}} = \frac{\Delta}{2} \sum_{E_i - E_j = \hbar\omega} \langle i | \sigma_\lambda | j \rangle | i \rangle \langle j |, \qquad (11)$$

where  $\sigma_{+(-)}$  are the qubit Pauli raising and lowering operators and  $i, j \in \{0, 1\}$  are the qubit persistent current state index. The low- and high-frequency parts of the noise give a convolutional form for the PSD in the polaron frame

- Landau, L. D. Zur Theorie der Energieubertragung II. Phys. Z. Sowjetunion 2, 46–51 (1932).
   Zener, C. Non-adiabatic crossing of energy levels. Proc. R. Soc. London, Ser. A 137, 696–702 (1932).
   Majorana, E. Atomi orientati in campo magnetico variabile. Nuovo. Cim. 9, 43–50 (1932).
   Stückelberg, E. C. Theory of inelastic collisions between atoms, using two simultaneous differential equations. Helv. Phys. Acta 5, 369–422 (1932).
- [2] Nikitin, E. E. & Umanskii, S. Y. Theory of Slow Atomic Collisions, vol. 30 of Springer Series in Chemical Physics (Springer Berlin Heidelberg, 1984).
- [3] Hänggi, P., Talkner, P. & Borkovec, M. Reaction-rate theory: Fifty years after Kramers. *Rev. Mod. Phys.* 62, 251–341 (1990).
- [4] Leuenberger, M. N., Meier, F. & Loss, D. Quantum Spin Dynamics in Molecular Magnets. In Linert, W. & Verdaguer, M. (eds.) *Molecular Magnets Recent Highlights*, 101–117 (Springer, 2003).
- [5] Ao, P. & Rammer, J. Quantum dynamics of a two-state system in a dissipative environment. *Phys. Rev. B* 43, 5397–5418 (1991).
- [6] Kayanuma, Y. & Nakayama, H. Nonadiabatic transition at a level crossing with dissipation. *Phys. Rev. B* 57, 13099–13112 (1998).
- [7] Oliver, W. D. et al. Mach-Zehnder Interferometry in a Strongly Driven Superconducting Qubit. Science 310, 1653–1657 (2005).
- [8] Zenesini, A. et al. Time-Resolved Measurement of Landau-Zener Tunneling in Periodic Potentials. Phys. Rev. Lett. 103, 090403 (2009).
- [9] Troiani, F. et al. Landau-Zener Transition in a Continuously Measured Single-Molecule Spin Transistor. Phys. Rev. Lett. 118, 257701 (2017).
- [10] Zhang, S. S., Gao, W., Cheng, H., You, L. & Liu, H. P. Symmetry-Breaking Assisted Landau-Zener Transitions in Rydberg Atoms. *Phys. Rev. Lett.* **120**, 063203 (2018).
- [11] Zhu, G. Y. et al. Crossover between the adiabatic and nonadiabatic electron transfer limits in the Landau-Zener model. Nat. Commun. 12, 456 (2021).
- [12] Nalbach, P. & Thorwart, M. Landau-Zener Transitions in a Dissipative Environment: Numerically Exact Results. *Phys. Rev. Lett.* **103**, 220401 (2009).
- [13] Weiss, U. *Quantum Dissipative Systems* (World Scientific, 2012).
- [14] Kadowaki, T. & Nishimori, H. Quantum annealing in

$$\tilde{S}(\omega) = \hbar^2 \int \frac{\mathrm{d}\omega'}{2\pi} G_L(\omega - \omega') G_H(\omega'), \qquad (12)$$

where  $G_L$  and  $G_H$  are contribution from the low- and high-frequency noise respectively, given by

$$G_L(\omega) = \sqrt{\frac{\pi}{2\hbar^2 W^2}} \exp\left[-\frac{(\hbar\omega - 4\epsilon_p)^2}{8\hbar^2 W^2}\right]$$
(13)

$$G_H(\omega) = \frac{4S_{\Phi_z,\text{ohmic}}(\omega)I_p^2}{\hbar^2\omega^2 + 4S_{\Phi_z,\text{ohmic}}(0)I_p^2}.$$
(14)

the transverse Ising model. *Phys. Rev. E* 58, 5355–5363 (1998).

- [15] Crosson, E. J. & Lidar, D. A. Prospects for quantum enhancement with diabatic quantum annealing. *Nat. Rev. Phys.* 3, 466–489 (2021).
- [16] Wubs, M., Saito, K., Kohler, S., Hänggi, P. & Kayanuma, Y. Gauging a Quantum Heat Bath with Dissipative Landau-Zener Transitions. *Phys. Rev. Lett.* **97**, 200404 (2006).
- [17] Amin, M. H. S., Love, P. J. & Truncik, C. J. S. Thermally Assisted Adiabatic Quantum Computation. *Phys. Rev. Lett.* **100**, 060503 (2008).
- [18] Munoz-Bauza, H., Chen, H. & Lidar, D. A double-slit proposal for quantum annealing. *npj Quantum Inf.* 5, 51 (2019).
- [19] Sillanpää, M., Lehtinen, T., Paila, A., Makhlin, Y. & Hakonen, P. Continuous-Time Monitoring of Landau-Zener Interference in a Cooper-Pair Box. *Phys. Rev. Lett.* **96**, 187002 (2006).
- [20] Quintana, C. M. et al. Cavity-Mediated Entanglement Generation Via Landau-Zener Interferometry. Phys. Rev. Lett. 110, 173603 (2013).
- [21] Amin, M. H. S. & Averin, D. V. Macroscopic Resonant Tunneling in the Presence of Low Frequency Noise. *Phys. Rev. Lett.* **100** (2008).
- [22] Johansson, J. et al. Landau-Zener transitions in a superconducting flux qubit. Phys. Rev. B 80, 012507 (2009).
- [23] Yan, F. et al. The flux qubit revisited to enhance coherence and reproducibility. Nat. Commun. 7, 12964 (2016).
- [24] Quintana, C. M. et al. Observation of Classical-Quantum Crossover of \$1/f\$ Flux Noise and Its Paramagnetic Temperature Dependence. *Phys. Rev. Lett.* **118**, 057702 (2017).
- [25] Lanting, T. et al. Probing high-frequency noise with macroscopic resonant tunneling. Phys. Rev. B 83, 180502 (2011).
- [26] Albash, T., Boixo, S., Lidar, D. A. & Zanardi, P. Quantum adiabatic Markovian master equations. *New J. Phys.* 14, 123016 (2012).
- [27] Chen, H. & Lidar, D. A. HOQST: Hamiltonian Open Quantum System Toolkit (2020). arXiv:2011.14046.
- [28] Smirnov, A. Y. & Amin, M. H. Theory of open quantum dynamics with hybrid noise. New J. Phys. 20, 103037 (2018).
- [29] Boixo, S. *et al.* Computational multiqubit tunnelling in programmable quantum annealers. *Nat. Commun.* 7,

10327 (2016).

- [30] Dickson, N. G. *et al.* Thermally assisted quantum annealing of a 16-qubit problem. *Nat. Commun.* 4, 1903 (2013).
- [31] Albash, T. & Lidar, D. A. Decoherence in adiabatic quantum computation. *Phys. Rev. A* 91, 062320 (2015).
- [32] Bando, Y., Yip, K.-W., Chen, H., Lidar, D. A. & Nishimori, H. Breakdown of the weak coupling limit in experimental quantum annealing (2021). arXiv:2111.07560.
- [33] King, A. D. et al. Coherent quantum annealing in a programmable 2000-qubit Ising chain (2022). arXiv:2202.05847.
- [34] Rosenberg, D. et al. 3D integrated superconducting qubits. npj Quantum Inf. 3, 1–5 (2017).
- [35] Yost, D. R. W. et al. Solid-state qubits integrated with superconducting through-silicon vias. npj Quantum Inf. 6, 1–7 (2020).
- [36] Valenzuela, S. O. et al. Microwave-Induced Cooling of a Superconducting Qubit. Science 314, 1589–1592 (2006).
- [37] Kerman, A. J. Efficient numerical simulation of complex Josephson quantum circuits (2020). arXiv:2010.14929.
- [38] Mozgunov, E. & Lidar, D. Completely positive master equation for arbitrary driving and small level spacing. *Quantum* 4, 227 (2020).

# Supplementary Information: Dissipative Landau-Zener tunneling: crossover from weak to strong environment coupling

#### S1. WIRING

In Figure S1 we present a diagram of the room-temperature and cryogenic setup used in the experiments. The qubit flux bias for the x and z loops,  $\Phi_x$  and  $\Phi_z$ , are controlled by currents generated by a DC voltage source and a high bandwidth source, combined through a bias tee at the mixing chamber stage of the dilution refrigerator. The DC biases are supplied by Yokogawa GS 200 voltage sources through twisted pair cable and low-pass filtered to below 32 kHz to minimize noise. The high bandwidth components of the current are supplied by a 1 GHz arbitrary waveform generators (AWGs) (Keysight M3202A), through coaxial cables. The fast line coupling to  $\Phi_x$  suffered from a cold open during the cooldown and is not used for the Landau-Zener experiment. The attenuators and filters on the cable are chosen to allow a sufficiently large current range for driving Rabi oscillation and performing annealing

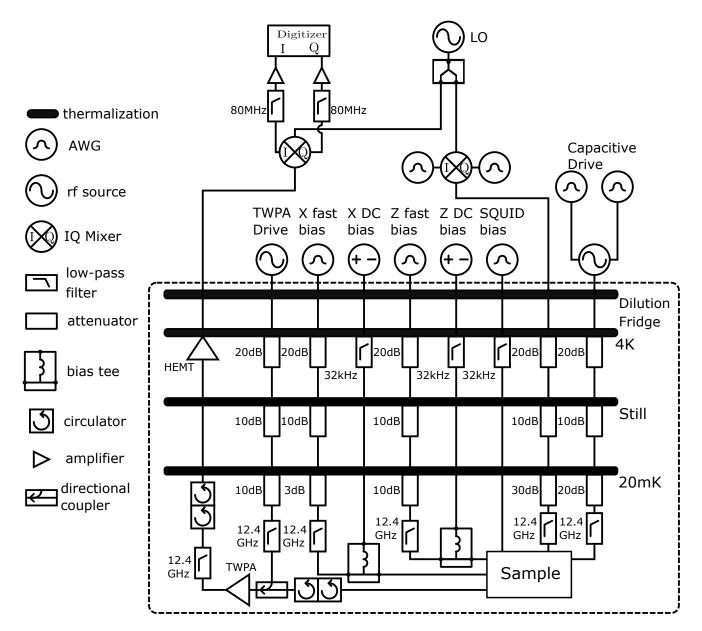


FIG. S1. Schematic of the setup used for experiments.

$L_r$	16.4pH
$L_l$	16.4pH
$L_z$	799.8pH
Icr	77.6nA
I <sub>cl</sub>	89.1nA
I <sub>c1</sub>	244.7nA
$I_{c2}$	244.7nA
$C_{ m cd}$	0.4fF
$C_{ m ad}$	3.6fF
$C_{ m ac}$	0.04fF
$C_{ m ab}$	14.2fF
$C_{ m gd}$	44.1fF
$C_{ m gc}$	0.2fF
$C_{ m ga}$	141.4fF
$C_{ m gb}$	90.0fF
SQUID inductance $L_s$	238.7pH
SQUID junction $I_s$	1187nA
resonator length $l_r$	$3.364 \mathrm{mm}$
Mutual between qubit and SQUID ${\cal M}$	60.3pH

TABLE I. Fit model best parameters for the qubit and resonator circuits.

experiment, while minimizing decoherence due to thermal and electronic noise. The resonator SQUID bias is supplied by an AWG (Keysight M3202A), but through twisted pair cable. The qubit can be driven with a capacitively coupled driving line, supplied by an rf source with an integrated IQ modulator, through a coaxial cable. The readout signal is amplified by a travelling wave parametric amplifier (TWPA) [S1] at the mixing chamber stage of the fridge, followed by a high-electron mobility transistor amplifier (HEMT) at the 4K stage, and room temperature amplifiers, before being processed by a field-programmable gate array (FPGA) digitizer (Keysight M3102A).

## S2. CROSSTALK CALIBRATION

DC flux crosstalk between different bias lines and flux loops are calibrated using the CISCIQi method developed in Ref. [S2]. We first measure the flux bias dependent resonator spectrum and the crosstalk into the resonator from other bias lines. This allows us to fix the resonator bias to measure the qubit-bias dependent transmission through the resonator. The procedure is iterated a few times until the crosstalk is compensated to within  $1 \text{ m}\Phi_0$  accuracy. The full crosstalk matrix is shown in Figure S2(a).

Crosstalk from the fast pulses sent to the qubit z loop to other loops are not compensated due to bandwidth limitations on other bias lines. For the small pulse amplitude used for the Landau-Zener sweep, reaching up to  $10 \text{ m}\Phi_0$ , the induced flux on the x, r loop should be inconsequential.

#### S3. CIRCUIT MODEL

The device used in this experiment consists of a capacitively-shunted flux qubit coupled to a tunable rf-SQUID terminated resonator. The coupling between these two circuits is done via the mutual inductance between the qubit z loop and the rf-SQUID loop. A lumped element representation of the qubit and resonator circuit is shown in Figure S2(b). The qubit eigenstates and eigenvalues are obtained using the numerical tools developed in Ref. [S3]. The circuit persistent current  $I_p$  and gap  $\Delta$  were verified experimentally via qubit spectroscopy, as shown in Figure S2(c). The simulated  $I_p$  and  $\Delta$  values are plotted as a function of  $\Phi_x$  in Figure S2(d).

The parameters of the resonator rf-SQUID were determined from fitting the experimental values of the resonator frequency versus resonator flux bias  $\Phi_r$ , shown in Figure S3(a). The resonator model allows for extraction of the value of the screening current in the rf-SQUID, which was used to determine the shift in the symmetry point of the qubit, induced by the rf-SQUID when biased away from zero. In order to confirm this value experimentally, spectroscopy curves were taken at a fixed value of  $\Phi_x$  at two different values of resonator bias  $\Phi_r$  at zero and -0.15, the value used for persistent current readout. The two spectroscopy curves are shown in Figure S3(b). The circuit parameters are summarized in Table I.

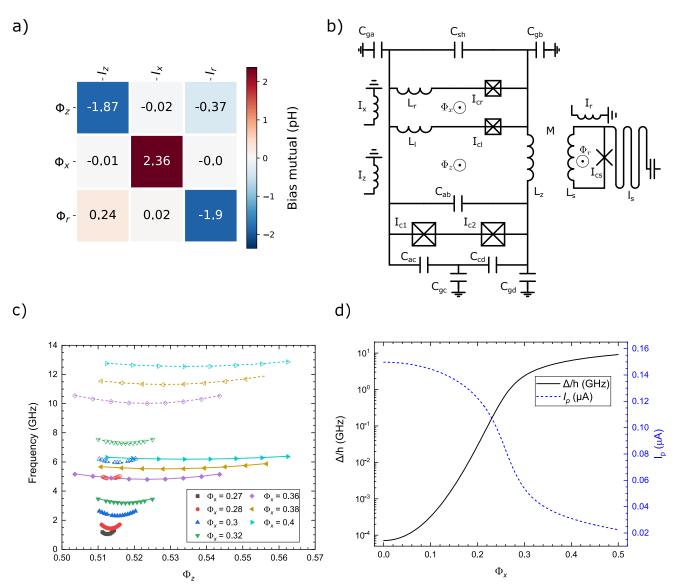


FIG. S2. a) Matrix of mutual inductances between on chip bias lines and flux loops. b) Circuit diagram for the qubit and coupler. c) Experimentally measured qubit transition frequency and simulated qubit transition frequencies for the best fit parameters, as a function of the biases  $\Phi_x$  and  $\Phi_z$ , and comparison with experiment. Filled symbols (solid lines) correspond to the experimentally obtained (simulated) transition frequencies between the ground and first excited state. Open symbols (dashed lines) correspond to the experimental (simulated) transition frequencies between the ground and second excited state. d) Simulated minimum gap (left axis, solid curve) and persistent current (right axis, dashed curve) values as a function of the bias  $\Phi_x$ .

## S4. FAST FLUX LINE COUPLING CHARACTERIZATION

As described in Section S1, fast voltage pulses are applied to the qubit z loop via a bias tee in order to control the flux bias of the qubit during the Landau-Zener sweep. In order to determine the transfer function between the voltage of the AWG and the flux fed to the qubit loop, a procedure using Ramsey interferometry was used.

The protocol is shown in Figure S4(a). Two  $\pi/2$  pulses are applied using the capacitively coupled waveguide, separated by the time  $\tau_{delay}$ . During the interval between the two  $\pi/2$  pulses, a trapezoidal flux pulse with 1 ns rise and fall time is applied to the z loop of the qubit. This flux pulse adiabatically changes the qubit frequency, depending on the pulse amplitude and duration, which induces an additional phase for the superposition created by the first  $\pi/2$  pulse, inducing an oscillation whose period depends on the flux amplitude. An example is shown in Figure S4(b) for the case of no flux pulse applied (i.e. pure Ramsey with no detuning) and with a 60 mV pulse applied.

The above sequence is repeated at a range of pulse amplitudes such that the detuning varied between approximately

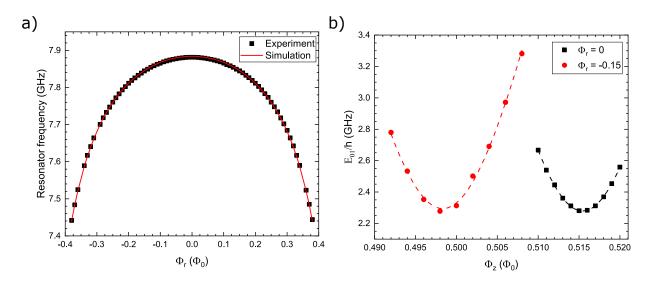


FIG. S3. a) Readout resonator resonance frequency vs bias: experiment (solid points) and simulation with best fit parameters (solid line). b) Experimentally measured shift of the qubit z symmetry point due to the SQUID screening current. Solid symbols correspond to qubit frequencies determined from spectroscopy, and dashed lines correspond to a fit using a two-level system anticrossing relation.

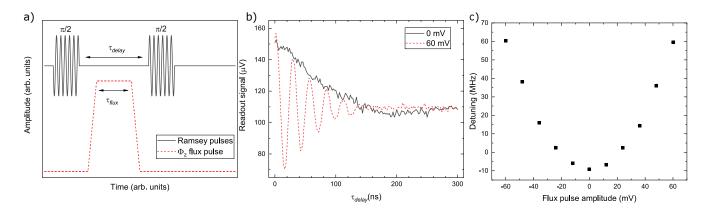


FIG. S4. Bias line characterization using a Ramsey protocol. a) Pulse sequence for Ramsey measurements. The qubit is initialized in a superposition using a  $\pi/2$  pulse, then a flux pulse applied to the qubit Z bias adiabatically detunes the qubit away from the symmetry point. The spacing between the two  $\pi/2$  pulses  $\tau_{delay}$  equal to the pulse duration  $\tau_{flux}$  plus the rise and fall times. The qubit acquires a phase dependent on the amplitude and duration of the pulse. b) Ramsey oscillation curves with  $V_z = 0$  and 60 mV. c) Fitted detuning as a function of pulse amplitude.

from 0 to 60 MHz. This detuning versus flux pulse amplitude is shown in Figure S4(c). Combining the detuning and the drive frequency gives the effective qubit frequency during the delay time in the Ramsey sequence. Comparing the qubit frequency versus flux pulse amplitudes allows us to deduce the voltage to flux conversion for the fast flux line.

## S5. FAST FLUX LINE PULSE DISTORTION CHARACTERIZATION

During the Landau-Zener measurement sequence, time-dependent flux pulses are applied to the qubit via a bias tee, as discussed in Sections S1 and S4. As the experiment involved the application of long pulses (duration > 1  $\mu$ s), we characterize the transmission of the AC port of the bias tee to check for possible frequency dependent attenuation effects that would distort the pulse shape.

In order to check for distortion effects, we used an experimental protocol based on a Ramsey sequence, shown in Figure S5(a). Two microwave  $\pi/2$  pulses are applied with a fixed delay time  $\tau_{delay}$ . The delay time is chosen to correspond to the inflection point of one of the Ramsey oscillations, so that the readout signal is maximally sensitive, and responds linearly to changes in qubit frequency and hence the flux pulse amplitude. The spacing between the

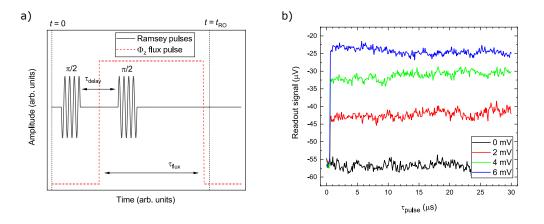
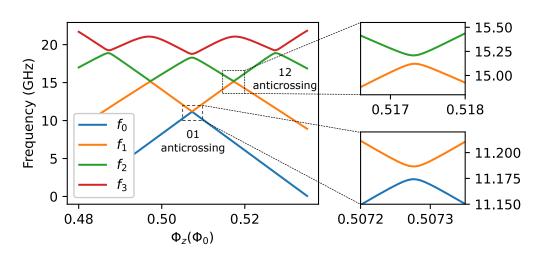


FIG. S5. Characterization of pulse distortion from the bias tee. a) Schematic of Ramsey-based sequence used to quantify the pulse distortion. b) Readout voltage as a function of pulse duration  $\tau_{\text{flux}}$ . The flat profile of the readout voltages out to several tens of  $\mu$ s shows that the bias tee negligibly distorts the pulse shape.



Circuit Spectra at  $\Phi_x = 0.185 \Phi_0$ 

FIG. S6. Energy Spectrum of the qubit circuit at  $\Phi_x = 0.185\Phi_0$ , with close up of the 01 and 12 anticrossing

Ramsey sequence and readout is fixed. In addition, a square pulse from  $\Phi_z$  fast line is applied with duration  $\tau_{\text{flux}}$ . The position of the rising edge of the square pulse is varied, spanning a range of times relative to the Ramsey pulses, from the rising edge following the first  $\pi/2$  pulse to preceding the first  $\pi/2$  pulse. This is done by increasing  $\tau_{\text{flux}}$  while keeping the falling edge and the Ramsey pulses at a fixed position relative to the readout pulse.

The readout signal as a function of pulse duration is shown in Figure S5(b) for several values of pulse amplitudes. For short pulse duration, the pulse starts after the Ramsey sequence and does not change the readout signal. As the pulse duration increases, the leading edge of the pulse moves past the second and then the first  $\pi/2$  pulse. The flux pulse experienced by the qubit in between the two  $\pi/2$  pulses changes the phase of the Ramsey oscillation, causing a sharp change in the measured signal, with width corresponding to  $\tau_{delay}$ . The Ramsey signal shown in Figure S5(b) is flat up to a pulse duration as long as 30  $\mu s$ , indicating that the pulse is negligibly distorted at these time scales.

## S6. STATE PREPARATION AND READOUT CALIBRATION

In this section, we describe the protocol for preparing the qubit in its ground state and the method for calibrating the readout voltage to obtain the state populations.

The qubit can in general be prepared in the ground state by waiting long enough. However, for some of the small

gap  $\Delta$  values used in the Landau-Zener experiments, the transition rate between the ground states of the two wells is very slow. Therefore, to prepare the qubit in the ground state before the Landau-Zener measurements, we use a sideband cooling method similar to that used in Ref. [S4] A plot of the qubit energy levels is shown in Figure S6. The qubit is prepared in its ground state at a bias about  $\Phi_z - \Phi_{z,\text{sym}} \approx 0.005$  away from the symmetry point, as follows. A sinusoidal pulse is applied which, on its positive side, sweeps the qubit further away from the symmetry point and past the anti-crossing between the first and second excited states. Prior to this sinusoidal pulse, the qubit is in a mixture of the ground and excited states. Due to the larger anti-crossing between the higher levels, the excited state can be adiabatically transferred into the same well as the ground state, which allows fast relaxation back to the ground state. By repeated sweeping across the anti-crossing between the first and second excited state, it is possible to prepare the qubit in the ground state. In our experiments, the qubit was cycled 5-10 times in order to prepare the ground state prior to the Landau-Zener sweep.

Next, we discuss the calibration of the readout signal. Given a fixed readout frequency, the transmission measured is given by a complex number  $V_g(V_e)$  for the qubit at the ground (excited) state. For a qubit in the mixed state, the readout voltage is given by  $V = V_g + P_e(V_e - V_g)$  where we assume populations beyond the qubit states are negligible. Therefore to obtain the qubit excited state population we need to obtain  $V_g$  and  $V_e$ .

For the Landau-Zener measurements  $V_g$  and  $V_e$  are calibrated at each  $\Phi_x$ . To measure  $V_g$  we prepare the qubit in the ground state at the readout point (at the end of the Landau-Zener sweep) using the cooling procedure discussed above. To measure  $V_e$ , we prepare the qubit in the excited state by preparation in the ground state at the opposite side of the symmetry point, followed by a fast, 1 ns long, Landau-Zener sweep through the minimum gap. Taking the qubit model parameters and the coherent Landau-Zener formula, a 1 ns Landau-Zener is expected to lead to a final excited state probability larger than 99% for even the largest  $\Delta$  measured in our experiments.

### S7. NOISE PARAMETERS AND MASTER EQUATION SIMULATION

In this section we discuss the noise model used in the master equation simulation. We first introduce the general form of noise and then discuss some specificities regarding including them into the adiabatic master equation (AME) and polaron-transformed Redfield equation (PTRE). For reference, we also provide a comparison of the noise parameters used in this work with noises measured in three other flux-qubit based quantum annealing devices, as summarized in Table II.

As the qubit circuit has relatively large flux loops, we assume the flux noise in the qubit x and z loops are the dominant sources of noise. The noises lead to fluctuation in the circuit Hamiltonian via

$$\delta H_{\rm c}(\Phi_z, \Phi_x) = \sum_{\lambda \in \{\Phi_z, \Phi_x\}} \frac{\partial H_{\rm c}}{\partial \lambda} \delta \lambda.$$
(S1)

In particular for  $\lambda = \Phi_z$ , in the two level approximation  $\frac{\partial H_c}{\partial \Phi_z} = -I_p \sigma_z$ . Note here when the noise source is quantum,  $\delta \lambda$  is a quantum operator of the environment.

The noise power spectral density (PSD) due to  $\delta\lambda$  is given by the Fourier transform of its auto-correlation function,

$$S_{\lambda}(\omega) = \int_{-\infty}^{\infty} \mathrm{d}\tau e^{i\omega\tau} \langle \delta\lambda(\tau)\delta\lambda(0) \rangle.$$
(S2)

Various previous measurements have shown that flux noise has roughly 1/f dependence, with f being frequency, up to around 1GHz, and then a quasi-ohmic spectrum at higher frequencies [S5–S7]. Furthermore, we follow Ref. [S6] to consider a quantum noise PSD with the positive and negative frequency components related by a phenomenological thermodynamic model. These considerations lead to the noise PSD given by

$$S_{\lambda} = S_{\lambda,1/f} + S_{\lambda,\text{ohmic}} \tag{S3}$$

$$S_{\lambda,1/f} = \frac{A_{\lambda}\omega}{|\omega|^{\alpha}} \left[ 1 + \coth\left(\frac{\beta\hbar\omega}{2}\right) \right],\tag{S4}$$

$$S_{\lambda,\text{ohmic}} = B_{\lambda}\omega|\omega|^{\gamma-1} \left[1 + \coth\left(\frac{\beta\hbar\omega}{2}\right)\right],\tag{S5}$$

where  $\beta = 1/k_B T$  is the inverse temperature,  $A_{\lambda}, B_{\lambda}$  determines the noise strength and  $\alpha, \gamma$  determine the frequency dependence. For 1/f noise,  $\alpha = 1$  and for ohmic noise  $\gamma = 1$ . The temperature is assumed to be the base temperature of the fridge, T = 20 mK.

	This work	Quintana et. al <sup>a</sup>	DWave CJJ qubit <sup>b</sup>	DWave CCJJ qubit <sup>c</sup>
$A^*_{\Phi_z} (\Phi^2_0/\mathrm{Hz})$	$(8.7 \times 10^{-6})^2$	$\sim (5 \times 10^{-6})^2/2$	_	$(1.3 \times 10^{-6})^{2}/2$
$\alpha$	0.91	0.96 - 1.05		0.95
$I_p(\mu \mathbf{A})$	0.104 - 0.129	$\sim 0.5$		$\sim 1.0$
W/h(predicted)(GHz)	0.048 - 0.059	$\sim 0.16$		0.05
W/h(measured)(GHz)		$\sim 0.25$	2.6	1.4
$T_{\rm eff}({ m mK})^{\rm d}$	20	20	21	53
$\eta g^{2\mathbf{e}}$	$6.8 \times 10^{-6}$	$\sim 5 \times 10^{-5}$		$\sim 0.065 [\mathrm{S7}]$

<sup>a</sup> The numbers are based on Ref. [S6]

<sup>b</sup> The numbers are based on Ref. [S10] where the Landau-Zener experiment is performed.

<sup>c</sup> The numbers are based on Ref. [S7, S11]

 $^{\rm d}$  This is the effective temperature that describes the MRT data assuming low frequency noise is at thermal equilibrium.

<sup>e</sup>  $\eta g^2$  is defined such that, the system bath coupling is given as  $gA \otimes B$ , where A, B are norm-1 system and bath operators respectively and the noise PSD of B is given as  $S(\omega) = 2\pi\eta\hbar^2\omega \frac{\exp(-|\omega|/\omega_c)}{1-\exp(-\beta\hbar\omega)}$ . See for example Ref. [S12] for more details.

TABLE II. Comparison of noise parameters used for simulation in this work and other work using flux qubits for quantum annealing.

The parameters of 1/f noise are obtained via measuring the flux bias dependent Ramsey dephasing times. The Ramsey dephasing time probes symmetrized 1/f noise in the low frequency limit, satisfying  $\hbar\omega \ll k_B T$ . In this limit, we have

$$S_{\lambda,1/f}^{+}(\omega) = \frac{1}{2} \left( S_{\lambda,1/f}(\omega) + S_{\lambda,1/f}(-\omega) \right)$$
(S6)

$$\approx \frac{A_{\lambda}\omega}{|\omega|^{\alpha}} \frac{2}{\hbar\omega\beta} \tag{S7}$$

$$=A_{\lambda}^{*}\left(\frac{2\pi}{|\omega|}\right)^{\alpha},\tag{S8}$$

where we defined  $A_{\lambda}^* = 2A_{\lambda}/[\hbar\beta(2\pi)^{\alpha}]$  to relate to the more commonly used expression for 1/f flux noise, used in for example Ref. [S8]. Given the similarity between our device and the device used in Ref. [S8], we assume  $\alpha = 0.91$  and found  $A_{\Phi_z}^* = (8.7 \times 10^{-6})^2 \Phi_0^2/\text{Hz}$ ,  $A_{\Phi_x}^* = (5. \times 10^{-6})^2 \Phi_0^2/\text{Hz}$  fits the measured Ramsey dephasing time best. More details on the coherence characterization of this qubit will be discussed in a separate publication [S9].

The quasi-ohmic component of the flux noise mainly contributes to qubit relaxation. It is more difficult to give quantitative estimate of the quasi-ohmic noise power as it leads to similar flux bias dependence of relaxation rates as other noise sources, such as ohmic charge noise [S5, S6]. For this reason, we use the reported ohmic noise strength measured in Ref. [S6] and scale it according to the ratio of the 1/f noise strength at 1Hz between the two devices. This gives  $\gamma = 1$  and  $B_{\Phi_z} \approx 1.3 \times 10^{-30} \Phi_0^2/\text{Hz}^2$ ,  $B_{\Phi_x} \approx 4.1 \times 10^{-31} \Phi_0^2/\text{Hz}^2$ . These values give reasonable agreement with the qubit  $T_1$  relaxation times we have measured. In Table II, we also provide these numbers in terms of the dimensionless coupling constant  $\eta$  that is often discussed in spin-boson literature. We also want to note that the simulation result is largely unchanged if the ohmic component of the noise spectrum is not included.

## A. Effect of X-noise coupling

In the master equation simulations, noise from  $\Phi_x$  is not included. This is justified based on three considerations. Firstly, the noise power of  $\Phi_x$  is less than half the noise power in  $\Phi_z$ . Secondly, as plotted in Figure. S7, the matrix elements of the flux operators between the circuit energy eigenstates  $\langle \alpha | \partial H / \partial \Phi_x | \beta \rangle$  is smaller than  $\langle \alpha | \partial H / \partial \Phi_z | \beta \rangle$  by a factor of 50. Finally,  $\Phi_x$  noise only primarily leads to transverse noise assuming small  $\Phi_x$  and small x loop junction asymmetry. Previous studies suggested that for transverse noise to have similar dissipative effects, its coupling strength needs to at least about 1/10 of the longitudinal noise [S13]; this condition is far from being satisfied in our case.

## B. Adiabatic master equation (AME)

In order to implement in AME the noise PSD in Eq. (S3), additional low and high frequency cutoffs  $\omega_l$  and  $\omega_h$  are added to avoid divergence. This introduces  $S_{\Phi_z}^{AME}$ , the PSD used in AME simulations, defined as

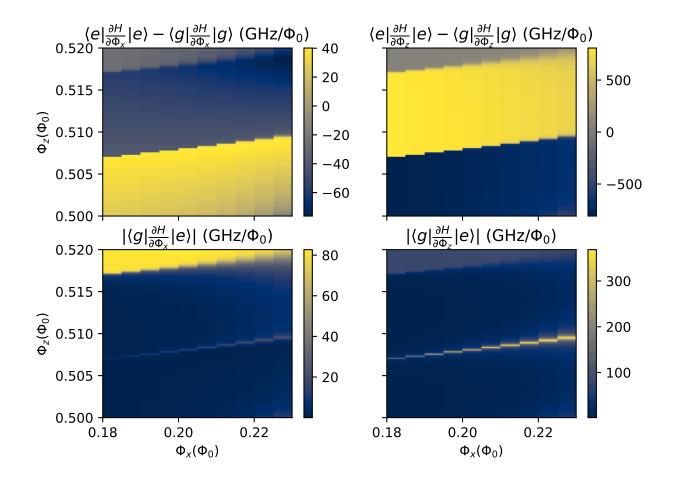


FIG. S7. Matrix elements for the x and z flux bias.

$$S_{\Phi_z}^{\text{AME}} = \begin{cases} S_{\Phi_z,1/f}(\omega) \exp\left(\frac{-|\omega|}{\omega_h}\right) + S_{\Phi_z,\text{ohmic}}(\omega) \exp\left(\frac{-|\omega|}{\omega_h}\right) & |\omega| > \omega_l \\ S_{\Phi_z,1/f}(\omega_l) \exp\left(\frac{-|\omega_l|}{\omega_h}\right) + S_{\Phi_z,\text{ohmic}}(\omega) \exp\left(\frac{-|\omega|}{\omega_h}\right) & |\omega| \le \omega_l. \end{cases}$$
(S9)

The high frequency cutoff is chosen to be  $\omega_h/2\pi = 10$ GHz, which is roughly the characteristic oscillation frequency in either of the qubit potential wells. For the low frequency cutoff, given that we are primarily concerned with thermalization effects, we choose  $\omega_l/2\pi = 10$ MHz, which corresponds to the minimum qubit frequency for the Landau-Zener measurement presented in this work.

## C. Polaron-transformed master equation (AME)

In the PTRE simulation, the noise model consists of an ohmic noise just as in AME, and the 1/f noise is represented by the MRT parameters W and  $\epsilon_p$  [S14]. The MRT width W characterizes the integrated effect of the symmetrized low frequency noise,

$$W^2 = 2I_p^2 \int_{\omega_{\text{low}}}^{\omega_{\text{high}}} \frac{d\omega}{2\pi} S^+_{\Phi_z,1/f}(\omega).$$
(S10)

The anti-symmetrized low frequency noise  $S^{-}_{\Phi_z,1/f}(\omega) = 1/2(S_{\Phi_z,1/f}(\omega) - S_{\Phi_z,1/f}(-\omega))$  gives the reorganization

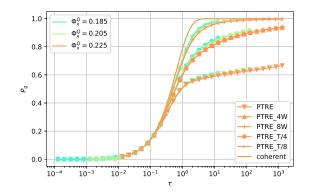


FIG. S8. Final ground state probabilities versus the dimensionless sweep time  $\tau = \Delta^2/\hbar v$  for different PTRE parameters.

energy  $\epsilon_p$ 

$$\epsilon_p = 2I_p^2 \int_{\omega_{\text{low}}}^{\omega_{\text{high}}} \frac{d\omega}{2\pi} \frac{S_{\Phi_z,1/f}^-(\omega)}{\hbar\omega}.$$
(S11)

For the integration limit, we choose  $\omega_{\text{low}}/2\pi = 4 \text{ Hz}$  based on the experiment time taken for all the repetitions at each  $\Phi_x$  and  $T_{\text{LZ}}$ , and  $\omega_{\text{high}}/2\pi = 10 \text{ Ghz}$  based on the characteristic oscillation frequency in the qubit potential wells. We assume that the low frequency noise is in thermal equilibrium, which relates W and  $\epsilon_p$  via the fluctuation dissipation theorem,  $W^2 = 2k_BT\epsilon_p$ . We also note that 1/f noise has a significant contribution to the noise power at high frequency, up to around 1 GHz. This contribution breaks the normalization condition for the high frequency noise in the current numerical implementation of PTRE (see discussion around Eq. [16] of Ref. [S15]). The effect of the high-frequency component of 1/f noise in the strong coupling limit is to be explored in future work.

As discussed in the main text, the values of W or T need to be adjusted for better agreement between PTRE simulation and the experiment data at low  $\Phi_x$ . The results are shown in Figure S8. Interestingly, it is found that increasing W by 4(8) times is equivalent to decreasing T by 4(8) times. This indicates that the ratio  $\epsilon/W$  is most critical to the result, with increasing  $\epsilon_p/W$  leading to closer to the coherent limit of ground state population.

#### D. Symmetric versus Asymmetric Landau-Zener Sweep

As discussed in Section S3, the screening current in the rf-SQUID leads to an effective bias to the qubit z loop. Due to an initial inaccurate estimation of this effect, the Landau-Zener data presented in the main text has an asymmetric scan range, with initial and final z loop bias being  $f_{z,\text{init}} = -3.1 \times 10^{-3}$  and  $f_{z,\text{final}} = 6.9 \times 10^{-3}$ . This was later identified via the spectroscopy method mentioned in Section S3, but leaving insufficient time to repeat the full range of Landau-Zener experiments. However, with this asymmetric scan range, the validity of the Landau-Zener model is not affected, since the initial and final longitudinal field are still much larger than the tunneling amplitude. In Figure S9, we compare the measured and simulated results for symmetric and asymmetric  $\Phi_z$  sweep range. The experiment data show some differences but the qualitative features discussed in the main text remain the same. In particular the symmetric data also show that as  $\Phi_x$  decreases,  $P_g$  becomes closer to the coherent limit behaviour. The simulated results using either AME or PTRE for the symmetric and asymmetric sweep range do not differ significantly.

<sup>[</sup>S1] Macklin, C. et al. A near-quantum-limited Josephson traveling-wave parametric amplifier. Science 350, 307–310 (2015).

<sup>[</sup>S2] Dai, X. et al. Calibration of Flux Crosstalk in Large-Scale Flux-Tunable Superconducting Quantum Circuits. PRX Quantum 2, 040313 (2021).

<sup>[</sup>S3] Kerman, A. J. Efficient numerical simulation of complex Josephson quantum circuits (2020). arXiv:2010.14929.

<sup>[</sup>S4] Valenzuela, S. O. et al. Microwave-Induced Cooling of a Superconducting Qubit. Science 314, 1589–1592 (2006).

<sup>[</sup>S5] Yan, F. et al. The flux qubit revisited to enhance coherence and reproducibility. Nat. Commun 7, 12964 (2016).

<sup>[</sup>S6] Quintana, C. M. et al. Observation of Classical-Quantum Crossover of 1/f Flux Noise and Its Paramagnetic Temperature Dependence. Phys. Rev. Lett. 118, 057702 (2017).

<sup>[</sup>S7] Lanting, T. et al. Probing high-frequency noise with macroscopic resonant tunneling. Phys. Rev. B 83, 180502 (2011).

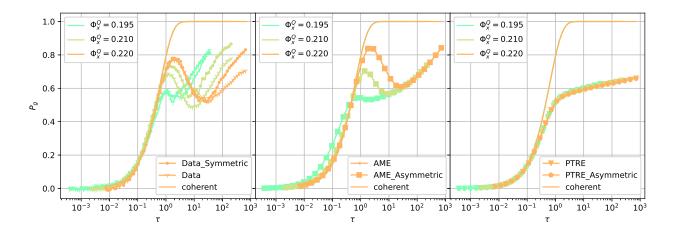


FIG. S9. Final ground state probabilities comparing the symmetric and asymmetric sweep around  $\Phi_z$  symmetry point, for experiment data on the left panel, AME simulation on the center panel and PTRE simulation on the right panel. The simulated results uses the nominal noise parameters discussed in Sec. S7 and the symmetric and asymmetric sweep overlap. The experiment data presented in the main text is asymmetric in range and the simulated data in the main text is symmetric in range.

- [S8] Weber, S. J. et al. Coherent coupled qubits for quantum annealing. Phys. Rev. Appl. 8, 014004 (2017).
- [S9] Trappen, R. et al. Decoherence in a tunable capacitively shunted flux qubit. (manuscript in preparation).
- [S10] Johansson, J. et al. Landau-Zener transitions in a superconducting flux qubit. Phys. Rev. B 80, 012507 (2009).
- [S11] Harris, R. et al. Experimental demonstration of a robust and scalable flux qubit. Phys. Rev. B 81, 134510 (2010).
- [S12] Albash, T., Boixo, S., Lidar, D. A. & Zanardi, P. Quantum adiabatic Markovian master equations. New J. Phys. 14, 123016 (2012).
- [S13] Javanbakht, S., Nalbach, P. & Thorwart, M. Dissipative Landau-Zener quantum dynamics with transversal and longitudinal noise. *Phys. Rev. A* 91, 052103 (2015).
- [S14] Amin, M. H. S. & Averin, D. V. Macroscopic Resonant Tunneling in the Presence of Low Frequency Noise. Phys. Rev. Lett. 100 (2008).
- [S15] Smirnov, A. Y. & Amin, M. H. Theory of open quantum dynamics with hybrid noise. New J. Phys. 20, 103037 (2018).